

This is the accepted manuscript made available via CHORUS. The article has been published as:

Carrier recombination dynamics in individual CdSe nanowires

Felix Vietmeyer, Pavel A. Frantsuzov, Boldizsar Janko, and Masaru Kuno

Phys. Rev. B **83**, 115319 — Published 16 March 2011

DOI: [10.1103/PhysRevB.83.115319](https://doi.org/10.1103/PhysRevB.83.115319)

Carrier recombination dynamics in individual CdSe nanowires

Felix Vietmeyer¹, Pavel Frantsuzov², Boldizsar Janko² and Masaru Kuno^{1,*}

¹Department of Chemistry and Biochemistry, ²Department of Physics, University of
Notre Dame, Notre Dame, Indiana 46556

*mkuno@nd.edu

Abstract

Carrier dynamics in single CdSe nanowires (NWs) have been studied using various techniques. They include measurements of single wire emission intensities as a function of pump fluence, excitation intensity-dependent emission quantum yields and excited state lifetimes. Ensemble transient differential absorption studies of induced bleach dynamics have also been conducted. Results of these studies show super linear growth of the emission intensity as a function of excitation intensity. This is corroborated by single nanowire emission quantum yields that vary as a function of excitation fluence and range from 0.1% to values over 10%. At the same time, measured emission lifetimes are short (<100 ps) while the nanowire band edge bleach persists for over a nanosecond. To explain all of the abovementioned results, a kinetic model that accounts for both the nature of photogenerated carriers within the wires as well as their subsequent recombination dynamics has been developed.

PACS: 42.70.-a, 73.20.Hb, 7867Uh, 7867-n, 78.30.Fs, 78.55.-m

Introduction

Semiconductor nanowires (NWs) are an emerging class of materials that offer unique optical and electrical properties. Applications include polarization sensitive photodetectors^{1,2}, lasers³⁻⁵, light emitting diodes⁶, logic gates⁷ and solar cells.^{8,9} These uses illustrate the versatility of NW optical/electrical properties for developing next generation technologies.

In all cases, the ability to control NW carrier dynamics as well as recombination processes is key to realizing these applications. However, despite the fact that NWs have been readily employed in numerous proof-of-concept applications, associated carrier recombination mechanisms remain to be more thoroughly explored. Among important properties not yet fully characterized are emission/carrier lifetimes, quantum yields, the effects of varying carrier densities and disorder along the NW length.

The present study therefore focuses on better elucidating room temperature carrier recombination mechanisms in solution-grown CdSe nanowires. Such materials have recently been developed as alternatives to VLS (vapor-liquid-solid)-grown wires. Among reasons for this, established solution-liquid-solid (SLS) syntheses yield crystalline NWs with narrow diameters that are within the confinement regimes of a number of important semiconductor systems. These preparations yield narrow diameter distributions (often between 15% and 25%) as well as lengths that exceed 1-10 μm . Resulting NWs are also passivated with ligands that datively bind to their surfaces. This provides steric as well as electronic stabilization to the wires. Furthermore, solution-based approaches allow for nanowires to be overcoated¹⁰⁻¹², opening up the possibility of creating core/shell systems that are potentially important for a number of applications.

CdSe is a particularly important model system since it's a well-studied bulk material. It also possesses an equally rich literature as colloidal quantum dots wherein much is now known about its excited state progression in the linear absorption, its band edge fine structure and its ultrafast carrier dynamics.^{13,14} More recently, CdSe NWs have been studied using optical spectroscopy.¹⁵⁻²³ This includes reports on spatially resolved NW emission spectra²⁰, theoretical and experimental measurements of their ensemble and single wire absorption cross sections^{21,22,24} as well as their polarization anisotropies.^{23,25}

Solution-grown CdSe NWs also exhibit other features that add complexity (and richness) to their optical properties. Namely, they exhibit zinc blende (ZB) and wurtzite (W) sequences within a given wire²⁶ due to the low energy difference between the two phases. Consequently, the wires likely possess intrawire Type-II disorder due to the presence of staggered band offsets.²⁰ As illustrations of potential disorder-induced phenomena, spectral heterogeneity²⁰ and emission flickering^{17,20} have recently been seen in individual CdSe nanowires. In all cases, the underlying cause of these phenomena still requires unraveling, further motivating our single wire studies.

We seek to comprehensively account for the following properties seen in CdSe NWs at both the ensemble and single wire levels. Namely,

- The observation of variable emission quantum yields, with reported values ranging from 0.1% to 20%.^{27,20}
- Excited state lifetimes on the order of 100 ps to 500 ps.¹⁵
- Ensemble transient differential absorption kinetics, showing nanosecond timescales.¹⁸

Towards this end, we have conducted a number of additional studies on CdSe nanowires. They include measurements of individual NW emission intensities as a function of pump fluence, measurements of their excitation intensity-dependent emission quantum yields as well as their excited state lifetimes. Ensemble transient differential absorption studies have also been conducted to monitor excited state carrier densities and recombination dynamics. The concerted use of these complementary methods has, in turn, enabled us to develop a kinetic model that begins to clarify the nature of photogenerated carriers and their recombination dynamics within the wires.

Results and discussion

As a first point of discussion, it's unclear whether photogenerated carriers are present in solution-based CdSe NWs as 1D-excitons or as free carriers. While CdSe's low bulk exciton binding energy of 15 meV²⁸ suggests the presence of free carriers at room temperature, Shabaev et. al.²⁹ as well as Muljarov et. al.³⁰ have predicted exciton binding energies as large as 300 meV due to dielectric contrast effects in narrow diameter NWs. However, experimental linear absorption measurements show apparent confinement-induced blue shifts of the band edge absorption with decreasing NW diameter.^{16,31} This possibly suggests the absence of *sizable* dielectric contrast effects since any increase in exciton binding energy simultaneously decreases the exciton Bohr radius and, in turn, retards the observed blueshifts.

Complicating this, ensemble transient absorption measurements suggest both excitonic and free carrier behavior in CdSe nanowires, depending on carrier density.¹⁸ Specifically, at low pump fluences both CdSe NWs and nanorods³² appear to exhibit

three-particle Auger kinetics. At higher pump fluences, a bimolecular process emerges possibly due to exciton-exciton annihilation. However, such a transition is neither predicted nor is well understood.

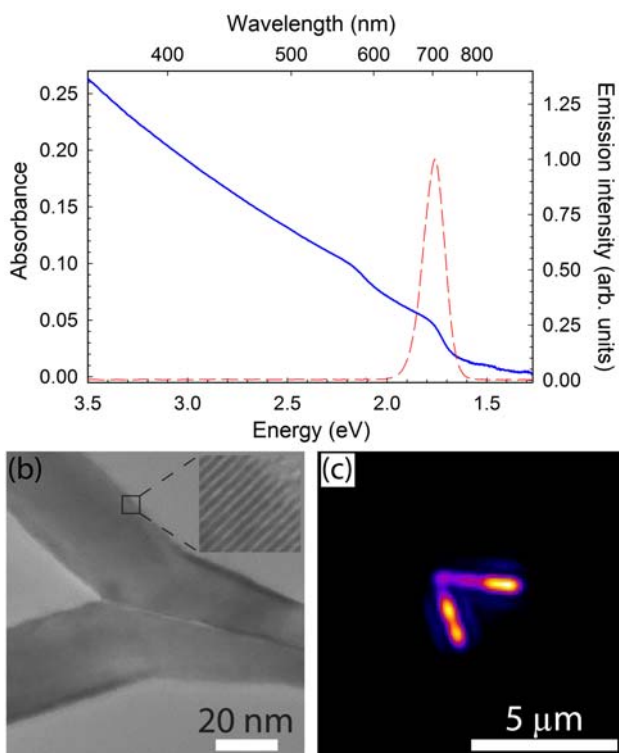


Figure 1: (a) Ensemble linear absorption (solid blue line) and emission spectrum (dashed red line) of CdSe nanowires. (b) TEM micrograph of the branching point in a “merge-y” NW. The inset in (b) illustrates the crystallinity of the material. (c) Emission microscopy image of a single NW. The observed $\sim 68^\circ$ angle is characteristic of the abovementioned “merge-y” NWs.^{22,33}

Figure 1a shows the ensemble absorption and emission of the wires studied. They possess a mean diameter of $d = 22$ nm ($\sigma = 40\%$) and have lengths up to 10 μm. To avoid any potential confinement effects and to simplify any subsequent analyses, large

diameter wires are investigated. This provides us a starting point for elucidating NW carrier dynamics. In addition, branched NWs within these ensembles are studied because they allow us to unambiguously select single nanostructures. Namely, a determination of whether single wires are being probed is made through the apparent morphology of the imaged specimen along with estimates of the expected signal, given known absorption cross sections and excitation intensities. Control experiments on straight nanowires were also carried out to confirm that branching points do not appear to impact the measurements presented herein. **Figure 1b** shows a TEM micrograph of one such wire, that illustrates both its morphology and its high degree of crystallinity. More about these wires and their various branched geometries can be found in References 33-37.

In our first experiment, changes in the emission intensity of single CdSe NWs are monitored as a function of excitation intensity. Previous studies have shown how such measurements can clarify the nature of carriers and their recombination mechanisms in low dimensional systems.³⁸⁻⁴¹ As an example, Reference 41 distinguishes free carrier dynamics from excitonic behavior based on the growth order of the emission intensity.

Consequently, in the current case, these measurements are used to help establish the nature of photogenerated carriers within the wires. In particular, a *linear* trend between the emission intensity and excitation intensity is expected in zeroth order, if the former simply reflects the increasing concentration of excitons within a wire. By contrast, when free carriers exist, the emission intensity should grow *quadratically* with pump fluence since the recombination of uncorrelated electrons and holes is intrinsically bimolecular.

Intensity-dependent measurements at several excitation wavelengths using continuous (CW) [405 nm (3.06 eV), 473 nm (2.62 eV), 532 nm (2.33 eV)] as well as pulsed [405

nm (3.06 eV), 550 nm (2.25 eV)] excitation were therefore conducted. These measurements show nonlinear growth of the emission intensity with excitation fluence, as illustrated in **Figures 2a** (CW) and **2c** (pulsed). Plots of the same data on log-log graphs yield straight lines, which, in turn, suggest power law growth of the intensity. The growth order can be seen through slopes extracted from linear fits to the data. They range from $m \sim 1.5$ to $m \sim 2$ [**Figure 2b** (CW) and **2d** (pulsed)]. The data's near-quadratic rise then suggests free carrier behavior, although the particular growth order remains to be explained (below).

In addition, the log-log plots show that emission growth under CW conditions is systematically slower than data taken under pulsed excitation conditions. Slopes of the former are close to $m \sim 1.7$ while they are near $m \sim 2$ in the latter. We find that the average slope using CW [pulsed] excitation is $m = 1.71$ (std. dev. = 0.09, sample size 10 points on 3 wires) [$m = 1.97$ (std. dev. = 0.15, sample size 10 points on 5 wires)].

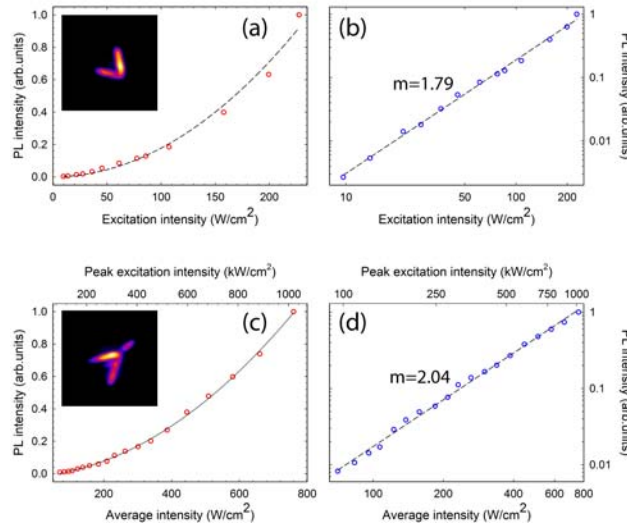


Figure 2: Emission intensity as a function of excitation fluence for two different single NWs under (a) CW and (c) pulsed (10 MHz) 405 nm excitation. In either case, the

dashed line is a fit to the data, illustrating the essentially quadratic nature of the growth. Accompanying logarithmic plots of the same data are shown for (b) CW and (d) pulsed excitation conditions. The dashed lines here are power law fits to the data and yield the actual nonlinear growth order through their exponents.

Corroborating this, we have measured single wire emission quantum yields with average NW quantum yields of $QY = 0.3\%$ (std. dev. = 0.2%) at low excitation intensities ($I_{exc} = 20 \text{ W/cm}^2$ at 405 nm, CW). This is consistent with previous estimates made under similar conditions.²⁰ Increasing the excitation fluence raises the average quantum yield to $QY = 1.5\%$ (std. dev. = 1.1% , $I_{exc} = 300 \text{ W/cm}^2$ at 405 nm, CW). Beyond this, even larger values are found [$QY = 4.6\%$ (std. dev. = 4.6% , $I_{exc} = 3000 \text{ W/cm}^2$ at 405 nm, CW)] and QY s greater than 10% are seen for approximately 20% of the wires studied. These large values are then in line with other reports, which have suggested NW QY s of this order.¹⁷ The strong excitation intensity dependence of NW QY s then accounts for the broad range of values reported in the literature.

To further link the emission intensity and quantum yield measurements to free carrier dynamics, time-resolved lifetime (TCSPC, time-correlated single photon counting) as well as transient differential absorption (TDA) measurements are carried out. Both allow us to characterize the timescales over which these carriers recombine. These experiments show rapid TCSPC decays as shown in **Figure 3** where a representative trace under low pump fluence conditions ($\langle I_{exc} \rangle = 13.5 \text{ W/cm}^2$, 405 nm, 10 MHz repetition rate with an associated peak intensity of $I_{exc} = 18 \text{ kW/cm}^2$) is plotted. In the figure, one sees a fast

initial decay that cannot fully be resolved despite an instrument response of ~ 100 ps (IRF, solid green line). This is true at all excitation intensities.

All acquired traces are dominated by this short decay component, which makes up $\sim 98\%$ of the total signal. However, longer lived contributions are present. Specifically, there exists a ~ 450 ps and a much longer ~ 2.5 ns component that make up $\sim 1.5\%$ and $\sim 0.5\%$ of the total signal. The ~ 450 ps contribution has previously been suggested to be the 1D exciton lifetime in CdSe.¹⁵ Similar values have also been predicted by Shabaev and Efros.²⁹

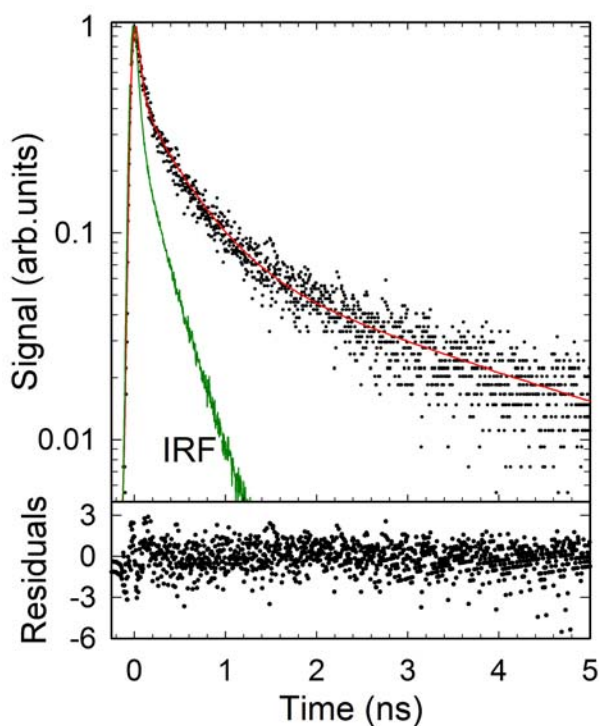


Figure 3: A representative TCSPC decay from a single CdSe NW using 70 ps pulses at 3.06 eV (405 nm). The signal at zero time is dominated by the ~ 100 ps instrument response function (IRF) (solid green line). A triexponential fit to the data using iterative reconvolution is provided. After ~ 300 ps, the decay becomes almost single exponential

with a fast (~ 450 ps lifetime) component and a much weaker slow (~ 2.5 ns lifetime) component. Residuals from the fit are provided below.

The observed fast excited state decay contrasts to previous transient differential absorption studies, which show nanosecond band edge bleach recoveries in CdSe NWs.¹⁸ To better clarify this difference in timescales, ensemble transient differential absorption measurements were therefore conducted on the same wires used above.

Figure 4b shows a representative (ensemble) transient differential absorption bleach profile taken on the same sample whose linear absorption is shown in **Figure 4a**. From a comparison of the spectra it is apparent that both show features at identical frequencies. This suggests band edge state filling and is supported by trends at higher pump fluences where the transient bleach broadens (**Figure 4b**, traces (3) and (4)). Similar behavior has been seen in CdS NWs and a more detailed analysis of the effect can be found in Reference 42.

Next, the band edge bleach recovery is monitored as a function of time. This allows us to study subsequent carrier recombination dynamics. On analyzing the resulting data, it's immediately apparent that, irrespective of whether small or large pump fluences are used, a long, sizable ns decay component exists in all traces (**Figure 5**). This is seen by clear offsets to the traces over the baseline even at times as long as 1.5 ns (the maximum delay imposed by the instrument's optical delay line). By contrast, we've already seen that the above emission lifetime measurements exhibit characteristic ~ 100 ps decays. Thus, a dramatic mismatch in timescales exists between the two measurements.

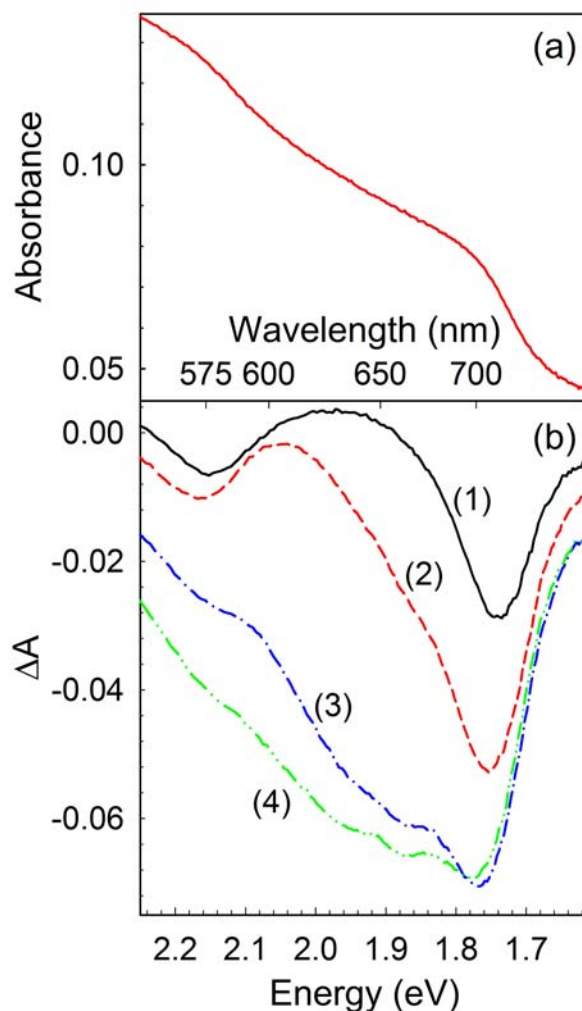


Figure 4: (a) Linear absorption spectrum of a CdSe NW ensemble. (b) Pump fluence-dependent transient absorption spectra shortly after excitation (~ 7 ps). Pump fluences increase from top to bottom: (1) $4 \mu\text{J}/\text{cm}^2$, (2) $12.2 \mu\text{J}/\text{cm}^2$, (3) $50.9 \mu\text{J}/\text{cm}^2$ and (4) $81.5 \mu\text{J}/\text{cm}^2$.

This mismatch can be rationalized by the fact that the transient bleach's magnitude depends on the carrier concentration in the NW's conduction and valence bands. However, due to the different CdSe electron and hole effective masses as well as differences in their accompanying density of states, the dominant bleach contribution

likely arises from the electron.¹⁴ Thus, the induced bleach predominantly reflects the conduction band electron population. Given this, electron recovery kinetics can be monitored using TDA.

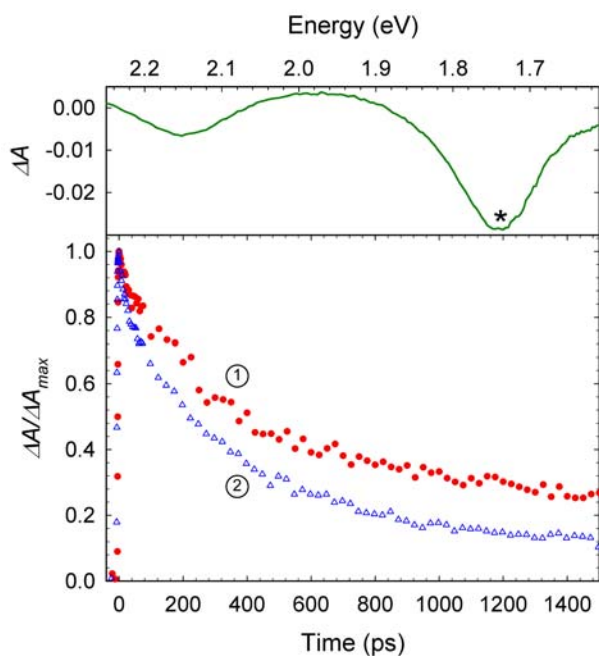


Figure 5: Kinetic traces of the bleach recovery taken at the maximum of the band edge bleach (denoted by an asterisk above) with pump fluences of (1) $4 \mu\text{J}/\text{cm}^2$ and (2) $50.9 \mu\text{J}/\text{cm}^2$.

In particular, **Figure 5** shows the recovery of the band edge transient as a function of time for two different excitation fluences. The data show dynamics on two timescales, as revealed by phenomenologically fitting the data to biexponential functions (not shown). Extracted timescales are on the order of $\approx 100 - 300$ ps and $\approx 1 - 3.5$ ns for pump fluences ranging from $2 \mu\text{J}/\text{cm}^2$ to $80 \mu\text{J}/\text{cm}^2$. However, the traces are strongly sensitive to excitation fluence. The two apparent timescales therefore change noticeably with increasing I_{exc} . This sensitivity suggests that an underlying higher order process must be

responsible for the TDA decays. In this regard, previous studies¹⁸ have invoked multiple carrier Auger processes and more about this will be seen below.

Kinetic model

To more quantitatively account for the aforementioned carrier recombination dynamics, we now develop a model to rationalize all of the above results in a self consistent manner. Of particular interest is to show that rapid hole trapping can readily explain the apparent order of magnitude difference in timescales between the band edge bleach kinetics (**Figure 5**) and the fast TCSPC decays (**Figure 3**). The model must also account for the super linear growth of the emission intensity with pump fluence as well as intensity-dependent changes in the NW quantum yield.

Figure 6 summarizes the model we propose and highlights the various radiative and nonradiative decay pathways assumed. We account for the generation of carriers via laser excitation and their subsequent bimolecular radiative recombination through paths 1 and 2. We also assume that both electrons and holes trap into defect states. This is denoted by paths 4 and 5. Trapped holes can recombine with free electrons (path 3) and with trapped electrons (path 6). The recombination of free holes and trapped electrons is excluded due to fast hole trapping along with slow electron trapping. To simplify the subsequent modeling we assume that radiative recombination only occurs between free electrons and free holes. In the absence of any apparent deep trap emission (**Figure 1**), trapped electrons and trapped holes recombine nonradiatively.

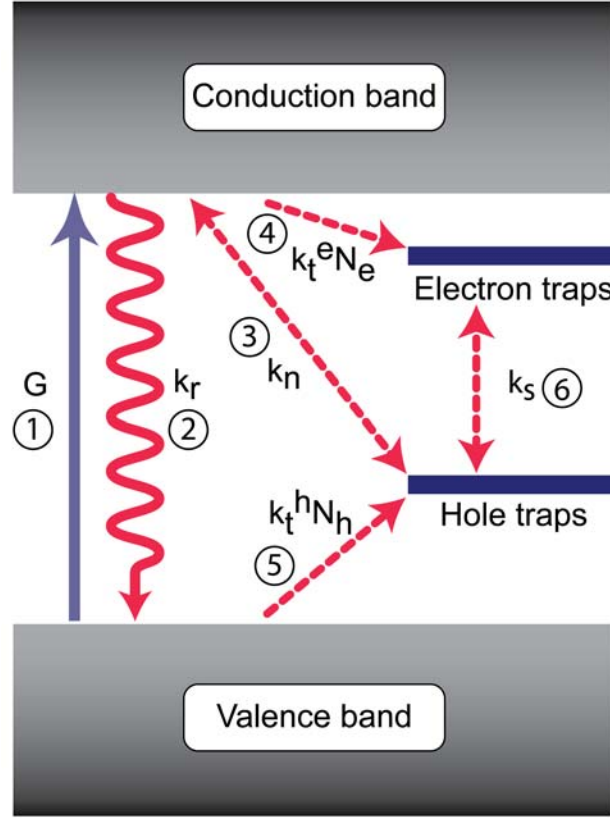


Figure 6: Illustration of the model described in the main text. Following generation, free carriers at the band edge recombine radiatively with a second order rate constant k_r . They can also be trapped with the effective first order rate constants $k_t^e N_e$ and $k_t^h N_h$. Additional nonradiative recombination channels involve trapped holes that recombine with free electrons (associated rate constant, k_n) as well as with trapped electrons (associated rate k_s).

The following differential equations are therefore used to describe the electron and hole concentrations in the NW's conduction and valence bands. Namely,

$$\frac{dn}{dt} = G - k_r np - k_n np_t - k_t^e N_e n \quad (1)$$

$$\frac{dp}{dt} = G - k_r np - k_t^h N_h p \quad (2)$$

$$\frac{dn_t}{dt} = k_t^e N_e n - k_s n_t p_t \quad (3)$$

$$\frac{dp_t}{dt} = k_t^h N_h p - k_n np_t - k_s n_t p_t \quad (4)$$

where n (p) is the electron (hole) concentration (i.e. number per unit length) at the conduction (valence) band edge and n_t (p_t) are their trapped concentrations. The following rate constants describe the various recombination processes invoked. Namely, k_r (k_n) is the second order radiative recombination rate constant (second order rate constant describing the recombination of free electrons and trapped holes), k_t^e (k_t^h) is the second order rate constant for electron (hole) trapping and k_s is the rate constant describing the nonradiative recombination of trapped electrons and trapped holes. N_e (N_h) is the number of electron (hole) traps. $G = \frac{I_{exc} \sigma}{h \nu}$ is an electron or hole generation rate and is determined by the product of the NW absorption cross section (σ) and the incident light intensity (I_{exc}) divided by the photon's energy. Equations 1-4 are only valid under situations where the concept of a carrier concentration holds. Thus, they fail in the limit of *very low* carrier densities.

The proposed model can then be used to rationalize our results by assuming nominal values for all rate constants. In particular, the literature suggests that hole trapping (path 5) in CdSe quantum dots occurs on a picosecond timescale.¹⁴ On the other hand, electron trapping can be much slower with an upper limit in the ms range.^{43,44} Since the trap number densities N_e and N_h are unknown, we simply employ the effective first order rate constants $k_t^e N_e$ and $k_t^h N_h$. Furthermore, in the absence of bimolecular *radiative*

recombination rates, we choose a rate constant similar to experimental values assigned for excitonic recombination in CdSe NWs.¹⁵ Although values for the trapped electron/trapped hole recovery rate, k_s , are not known, we speculate that this process occurs on much slower timescales than both radiative recombination (path 2) and hole trapping (path 5). For modeling purposes, we ultimately assume that k_s represents a second order process. Values for k_n are also not known, although we will assume an associated rate smaller than that connected with hole trapping. At very high intensities, this rate may become significant due to large trapped hole populations. Our assumed kinetic rate constants are therefore:

- $k_t^h N_h \sim 100 \text{ ns}^{-1} (1 \times 10^{11} \text{ s}^{-1})$
- $k_t^e N_e \sim 0.01 \text{ ns}^{-1} (1 \times 10^7 \text{ s}^{-1})$
- $k_n \sim 0.0032 \text{ } \mu\text{m ns}^{-1} (3.2 \times 10^2 \text{ cm s}^{-1})$
- $k_r \sim 0.01 \text{ } \mu\text{m ns}^{-1} (1 \times 10^3 \text{ cm s}^{-1})$
- $k_s \sim 0.0001 \text{ } \mu\text{m ns}^{-1} (10 \text{ cm s}^{-1})$.

CW experiments

With this, we first attempt to explain the super linear growth of I_{emm} (**Figure 2**) as well as the QY growth with excitation intensity for three I_{exc} regimes. In the model, at very low excitation fluences, carrier trapping via paths 4 and 5 and subsequent non-radiative recombination dominate the electron/hole decay kinetics following generation. Under these conditions, Equations 1 and 2 simplify to

$$\frac{dn}{dt} \approx G - k_t^e N_e n \quad (5)$$

$$\frac{dp}{dt} \approx G - k_t^h N_h p. \quad (6)$$

Steady-state solutions to these equations yield $n = \frac{G}{k_t^e N_e}$ and $p = \frac{G}{k_t^h N_h}$ such that $n \propto G$ and $p \propto G$. Since the NW emission intensity is proportional to the radiative rate ($I_{emm} \propto k_r np$), we find that $I_{emm} \propto k_r np = \frac{k_r G^2}{k_t^e N_e k_t^h N_h}$. As a consequence, I_{emm} grows quadratically with pump fluence. This is shown in **Figure 7** where plotting I_{emm} versus I_{exc} on a log-log plot yields linear behavior with a slope of $m=2$ (dashed line, bottom left). This is similar to the data in **Figure 2b**, which has a near identical slope. The deviation from $m=2$ is explained shortly. Next, given that the quantum yield is proportional to the ratio of emitted to absorbed photons ($QY = \frac{k_r np}{G} \propto G$) it grows linearly with excitation intensity. This is also supported by our experimental measurements which show a steady rise of the measured QY with I_{exc} .

Next, at higher excitation intensities, path 3 dominates path 4. As a consequence, in this regime, we approximate Equations 1 and 2 as

$$\frac{dn}{dt} \approx G - k_n np_t \quad (7)$$

$$\frac{dp}{dt} \approx G - k_t^h N_h p. \quad (8)$$

This, in turn, implies $n \approx p_t$. As a consequence, steady-state solutions to Equations 7 and

8 yield $p = \frac{G}{k_t^h N_h}$ and $n = \sqrt{\frac{G}{k_n}}$ such that $p \propto G$ and $n \propto \sqrt{G}$. This, again, leads to

nonlinear growth of the emission intensity since $I_{emm} \propto k_r np = \frac{k_r G^{1.5}}{k_t^h N_h \sqrt{k_n}}$. A log-log plot

of I_{emm} versus I_{exc} thus yields linear behavior with a slope of $m=1.5$ (**Figure 7**, dashed line, middle). **Figure 2b** again corroborates this prediction since the data exhibits a slope of $m=1.7$ which is intermediate between the prior low fluence ($m=2$) CW limit and the eventual ($m=1$) high fluence limit to be discussed in what follows. The corresponding quantum yield predicted by the model is $QY = \frac{k_r np}{G} = \frac{k_r G^{0.5}}{k_t^h N_h \sqrt{k_n}} \propto G^{0.5}$ and continues to increase with I_{exc} , albeit in a sublinear manner (**Figure 7**, inset).

Finally, at very large pump fluences radiative recombination ($k_r np$) is faster than hole trapping ($k_t^h N_h p$) and the free hole concentration, p , is sizable with $p > p_t$. Equations 1 and 2 become

$$\frac{dn}{dt} \approx \frac{dp}{dt} \approx G - k_r np \quad (9)$$

where $n \approx p$. The resulting steady state solutions are then $n \approx p = \sqrt{\frac{G}{k_r}}$. As a consequence, $n \propto \sqrt{G}$ and $p \propto \sqrt{G}$. The predicted emission intensity under these conditions is thus $I_{emm} \propto k_r np = G$ and grows linearly with excitation intensity with a log-log plot slope of $m=1$ (**Figure 7**, dashed line, top right). The associated QY is constant and reaches a hypothetical value of unity. Note that the model does not consider band filling or other high carrier density effects. In this limit, though, linear behavior along with less than unity QYs can be observed and would need to be explained by invoking additional effects. A detailed analysis of this high excitation intensity regime is left to future studies.

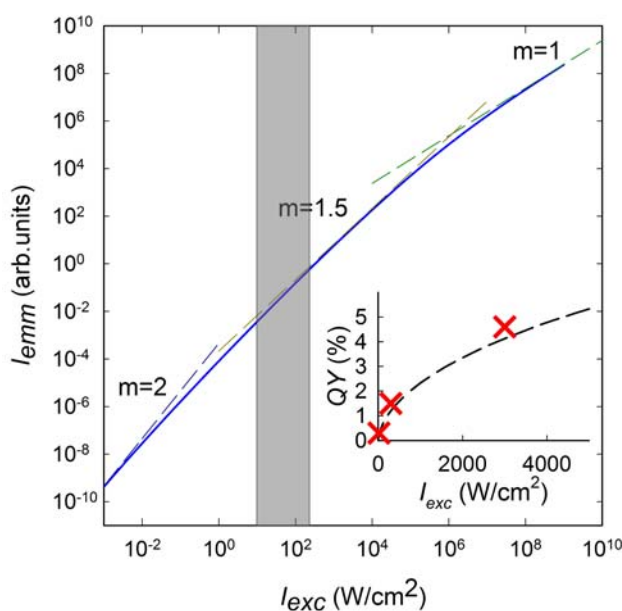


Figure 7: Theoretical log-log curve of I_{emm} as a function of I_{exc} as predicted by the model under CW conditions. At very low excitation fluences ($I_{exc} < 10 \text{ mW/cm}^2$) the slope is $m=2$ whereas at very high intensities ($I_{exc} > 100 \text{ MW/cm}^2$) $m=1$. The grey shaded region denotes the range of excitation intensities used in the current experiment. Dashed lines are guides to the eye and illustrate slopes of $m=1$, $m=1.5$ and $m=2$. The inset shows experimental quantum yields (red crosses) and predictions of the model (dashed line).

The full model curve is depicted in **Figure 7** as a solid black line. It is found by solving Equations 1-4 under steady-state conditions along with the prior rate parameters. One sees that it readily predicts I_{emm} versus I_{exc} slopes intermediate between $m=2$ and $m=1$ in the experimental range of interest. This is highlighted by the grey shaded region in **Figure 7**. Furthermore, the inset shows the corresponding model QY (calculated using

the relation $QY = \frac{k_r np}{G}$) as a function of I_{exc} along with measured experimental values.

Again it's apparent that the model qualitatively reproduces the observed trends.

Pulsed experiments

To continue developing our model predictions, we now consider the response of the system under pulsed excitation conditions, characteristic of TCSPC and TDA measurements. For simplicity, we assume instantaneous excitation of the NW in order to focus on subsequent carrier kinetics. We first consider low fluences when hole trapping (path 5, **Figure 6**) is much faster than radiative recombination (path 2, **Figure 6**). In addition, both electron trapping (path 4, **Figure 6**) and the recombination of free electrons with trapped holes (path 3, **Figure 6**) are relatively slow processes. With this,

$\frac{dn}{dt} \approx 0$ such that $n = n_0 = \left(\frac{I\sigma}{h\nu} \right) \tau_{pulse}$ with τ_{pulse} the laser pulse width. The free electron concentration is therefore constant at very short times. For holes, we have for similar reasons $\frac{dp}{dt} \approx -k_t^h N_h p$. Solving for $p(t)$ then yields $p(t) = p_0 e^{-k_t^h N_h t}$ with $p_0 \approx n_0$. The associated, short-time, emission intensity is therefore

$$I_{emm}(t) \propto k_r p(t) n(t) \approx k_r n_0^2 e^{-k_t^h N_h t} \quad (10)$$

and decays exponentially due to fast hole trapping.

The associated (average) emission intensity in these pulsed laser experiments is

$$\langle I_{emm} \rangle \propto f \int_0^\infty I_{emm}(t) dt = f k_r n_0^2 \int_0^\infty e^{-k_t^h N_h t} dt = \frac{f k_r n_0^2}{k_t^h N_h} \quad (11)$$

where f is the laser repetition rate ($f = 10$ MHz in our simulations). From $n_0 \propto G$, it follows that $\langle I_{emm} \rangle \propto G^2$. As a consequence, plotting $\langle I_{emm} \rangle$ versus $\langle I_{exc} \rangle$ yields a line with a slope of $m=2$. This is illustrated by the dashed line in **Figure 8** (bottom left) and again agrees well with the pulsed excitation results shown in **Figure 2d**. At the same time, the associated QY grows linearly with excitation intensity since $QY \propto \frac{\langle I_{emm} \rangle}{G} \propto G$. At high pump fluences, the model predicts unity QY (i.e. $\langle I_{emm} \rangle \propto G$) since all photogenerated carriers recombine via bimolecular radiative recombination (path 2, **Figure 6**). This corresponds to a slope of $m=1$ in log-log plots of $\langle I_{emm} \rangle$ versus $\langle I_{exc} \rangle$ (**Figure 8**, dashed line, top right).

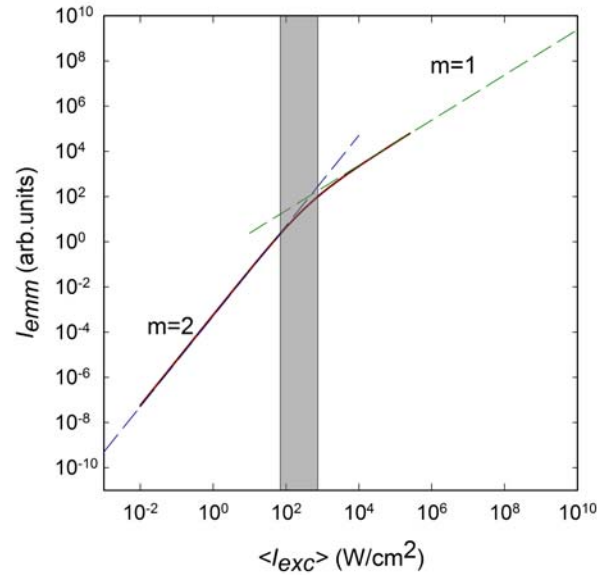


Figure 8: Theoretical log-log plot of $\langle I_{emm} \rangle$ versus $\langle I_{exc} \rangle$ under pulsed excitation conditions at 405 nm. Eventual saturation of the QY results in two effective regimes with slopes of $m=1$ and $m=2$. Dashed lines are guides to the eye.

The full model curve for pulsed excitation conditions is shown by the solid black line in **Figure 8**. It was generated by numerically solving Equations 1-4 using a Runge-Kutta algorithm with initial conditions $n(0)=p(0)=n_0$ and $n_t(0)=p_t(0)=0$. The resulting rate, k_rnp , was integrated with respect to time. One sees that the predicted slope at low fluences is $m=2$ while at very high fluences it changes to $m=1$. As with the CW case, the slope of $m=1$ implies a hypothetical unity QY. In practice, though, linear behavior and less than unity QYs can be explained by band filling and other high carrier density effects as outlined earlier.

Our model predictions are in good agreement with the results shown in **Figure 2d**. As in **Figure 7**, the grey shaded region denotes the range of excitation intensities used in actual experiments. Note though that since the model assumes instantaneous excitation conditions, whereas the measurements in **Figure 2d** involve a finite pulse width of 70 ps, the true experimental region of interest occurs at slightly lower intensities on this idealized intensity axis. The agreement between model and experiment therefore improves.

Finally, the model makes predictions about our ensemble TDA measurements. Underlying the analysis is the assumption that the kinetics of the observed transient bleach primarily reflect the conduction band electron dynamics. This is because we have previously argued that hole trapping is extremely fast. Furthermore, the different electron

and hole effective masses and their associated density of states suggest that electron kinetics are predominantly being monitored in TDA experiments.¹⁴

To qualitatively rationalize the data in **Figure 5**, we consider fast hole trapping on the ≈ 10 ps timescale such that subsequent electron dynamics are described by

$$\frac{dn}{dt} \approx -k_n np_t - k_t^e N_e n \quad (12)$$

where $p_t \approx n$. Two limiting cases exist. First, at very short times following hole

trapping path 4 in **Figure 6** is negligible. Thus $\frac{dn}{dt} \approx -k_n np_t$. Solving for the free

electron concentration then yields $n(t) \approx \frac{n_0}{(1 + n_0 k_n t)}$, which corresponds to the short time

contribution in our earlier fits. Next, at very long times, the dynamics of longer-lived

electrons are being monitored. As a consequence, $\frac{dn}{dt} \approx -k_t^e N_e n$. Solving for $n(t)$ then

gives $n(t) \approx n_0^* e^{-k_t^e N_e t}$ with n_0^* , the residual long-lived electron concentration following the nonradiative recombination of free electrons with trapped holes.

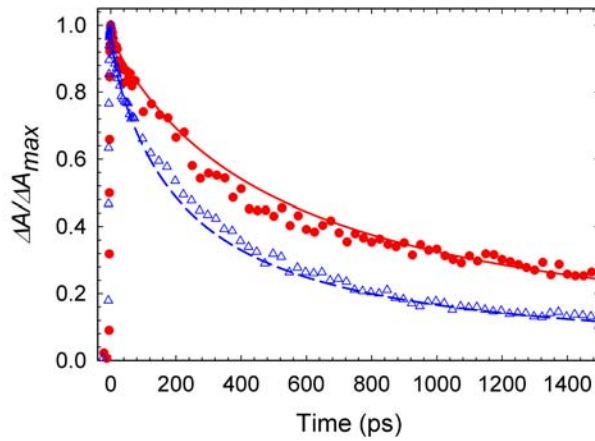


Figure 9: Theoretical band edge bleach recovery kinetics for two pump fluences, 4 $\mu\text{J}/\text{cm}^2$ (solid red line) and 50.9 $\mu\text{J}/\text{cm}^2$ (dashed blue line). For comparison purposes, the red dots (blue triangles) are experimental results from **Figure 5** obtained with identical pump fluences.

The model can, however, make more quantitative predictions. **Figure 9** shows the model's predicted TDA bleach recovery for two different pump fluences with an absorption cross section of $\sigma = 1.47 \times 10^{-10} \text{ cm}^2/\mu\text{m}$ at 3.20 eV (387 nm). To create this graph, a plot of ΔA_{max} versus pump fluence was first fit to the generic function $\Delta A_{\text{max}} = \frac{x}{1 + y/n_0}$ with x and y being fit parameters. This provides an appropriate relationship linking ΔA_{max} to n_0 across all pump fluences of interest. Equations 1-4 are then solved numerically using a Runge-Kutta algorithm and obtained $n(t)$ values are mapped onto ΔA magnitudes via the prior $\Delta A_{\text{max}}/n_0$ relationship.

Resulting curves for both pump fluences show a fast initial decay. We suggest that it arises from the recombination of free electrons with trapped holes (path 3, **Figure 6**) as seen earlier when discussing Equation 12. The longer-lived decay then arises from much slower electron trapping (path 4, **Figure 6**). As the excitation intensity increases, the overall kinetics speed up given the increasingly larger values of $k_n n p_t$. From **Figure 9**, it's apparent that the theoretical traces qualitatively reproduce the trends seen in the experimental data (symbols). Note that at the very largest pump fluences, an additional early time contribution to the fast decay kinetics comes from radiative recombination given the large p values implicit to this scenario. The bulk of the fast decay, however, is

still due to the nonradiative recombination of electrons and trapped holes (path 3, **Figure 6**).

As one final point of interest, the model potentially accounts for apparent variable order Auger kinetics previously invoked in TDA studies of CdSe NWs.¹⁸ Namely, the transition from a high pump fluence bimolecular recombination regime to a low fluence region where apparent three-carrier (3rd order) kinetics occur can be rationalized by **Equation 12**. Without going into great detail, note that at high pump fluences the TDA kinetics is predominantly bimolecular in nature due to the recombination of free electrons and trapped holes. At lower pump fluences, both terms in **Equation 12** contribute to the overall decay. As a consequence, deviations from bimolecular kinetics will occur and may lead to decays, which follow apparent 3rd order kinetics.¹⁸

Note that the second order rate constant we assign to the recombination of trapped holes and free electrons is nearly identical to that previously assigned to bimolecular exciton-exciton annihilation in 7 nm diameter CdSe NWs.¹⁸ However, we have also shown through preliminary studies that narrow-diameter nanowires (d=5 nm) such as the ones previously studied in TDA experiments¹⁸ do not show nonlinear growth of the emission intensity with excitation intensity (I_{exc} ranges from 70 – 14000 W/cm² at 473 nm) as expected for free-carrier recombination. This varied behavior then suggests that, unlike the bulk-like nanowires studied here, which clearly exhibit free-carrier behavior, narrow-diameter CdSe NWs may exhibit mixed excitonic as well as free carrier properties. Further studies are therefore needed to unambiguously identify the nature of carriers in these narrow-diameter CdSe NWs that are within their intermediate confinement regime.

Experimental Section

Nanowire synthesis

A detailed description of the nanowire synthesis can be found elsewhere.³⁴ Briefly, CdSe nanowires were synthesized using CdO and trioctylphosphine selenide (TOPSe) as precursors for Cd and Se. A mixture of CdO, octanoic acid (OA) and TOPO was degassed under nitrogen in a three neck flask. The reaction vessel was then heated until the cadmium complexed with the octanoic acid. This turned the reaction mixture clear. A solution of 1M TOPSe and Au/Bi catalyst nanoparticles²⁶ (or BiCl₃ for the in-situ preparation of the catalyst³¹) was then injected at temperatures between 240 °C and 300 °C to initiate NW growth.

The reaction was eventually stopped by cooling the mixture below 200 °C. Toluene was added to prevent TOPO from solidifying. A small amount of methanol induced the NWs to precipitate whereupon the suspension was centrifuged to isolate the wires. The recovered product was then resuspended in fresh toluene. A washing procedure, consisting of repeated precipitation and resuspension steps, was carried out 3-5 times to purify the NWs and to remove any quantum dots formed as byproducts during the synthesis.

In the current experiment, resulting wires possess a mean diameter of $d = 22$ nm ($\sigma = 40\%$) and have lengths ranging from 1 to 10 μm . NWs grow preferably along the $\langle 111 \rangle$ (ZB) and $\langle 0001 \rangle$ (W) directions of CdSe as documented earlier.³⁴ By altering both the metal-to-chalcogen stoichiometry as well as the growth temperature, various nanowire

morphologies can be made. More information about branched CdSe (and other) nanowires can be found in References 33-37.

Optical measurements

Calibration standard for quantum yield measurements.

Amine-modified microspheres (FluoSpheres, type F8763, $d = 210$ nm, $\lambda_{em} = 610$ nm) were purchased from Invitrogen and served as our quantum yield reference. To use the beads, the absorption cross section of a single bead was first determined using extinction measurements, assuming the vendor provided stock concentration (0.02 g/ml). The resulting single bead absorption cross section at 3.06 eV (405 nm) was $\sigma = 1.7 \times 10^{-10}$ cm². Next, a fluorimeter was used to estimate the emission quantum yield (QY) of the microspheres by referencing their integrated emission intensity to that of cresyl violet perchlorate in ethanol ($QY = 0.54$).⁴⁵ Both systems were excited at 2.30 eV (540 nm) with their absorbances matched at the excitation wavelength. Differences in solvent refractive indices as well as spectrometer sensitivities were taken into account. The resulting single bead quantum yield estimate is $QY = 15.6$ %.

Comparative quantum yield measurements.

For all NW QY measurements, the excitation source was a multimode 405 nm (3.06 eV) diode laser. Its output was spatially filtered with a pinhole and was subsequently attenuated with crossed linear polarizers. Measurements were carried out on a homebuilt inverted microscope, using a high N.A. oil immersion objective (Zeiss Plan-Apochromat, 100x, N.A. 1.4). The emitted light from either individual microspheres or NWs was

collected with the same objective and was passed through a barrier filter (Chroma HQ 500LP) to eliminate any residual excitation light. The sample was then imaged with a back-illuminated EMCCD camera (Andor, Model 897). By normalizing the integrated count rates to the cross section of single microspheres, NW QY s on fused silica were determined. Note that the estimated absorption cross section of a single $d = 22$ nm NW is $\sigma = 1.22 \times 10^{-10} \text{ cm}^2/\mu\text{m}$ at 3.06 eV (405 nm).²⁴ This value is consistent with both ensemble²¹ and more recent single NW cross section measurements.²²

NW power-dependent emission intensity measurements

Individual NW emission intensities were studied on fused silica in air as a function of pump fluence using multiple CW [405 nm (3.06 eV), 473 nm (2.62 eV) and 532 nm (2.33 eV)] and pulsed laser sources [405 nm (3.06 eV) and 550 nm (2.25 eV)]. Pulse durations at 405 nm were 70 ps at a repetition rate of 10 MHz (PicoQuant LDH-P-C 405) while those at 550 nm had a width of 10 ps at 40 MHz (Fianium SC-450). When using the latter excitation source, traces were taken on a separate microscope system based around a Nikon TE-2000U inverted frame. A barrier filter (Chroma, HQ 680LP) was used to filter the collected light and a single photon counting avalanche photodiode (APD, Perkin Elmer, SPCM AQR-14) served as the detector. All other traces were taken on the homebuilt microscope described above, using a barrier filter (Chroma, HQ 680LP) along with a separate single photon counting APD (PicoQuant, PDM series). In general, crossed linear polarizers were used to adjust the excitation fluence to a desired level. All optical measurements were carried out using variable wave plates to ensure the excitation's circular polarization just prior to the microscope objective.

Transient differential absorption measurements

Transient absorption measurements were carried out on a Clark-MXR CPA 2010 Ti:Sapphire system operating at 1.6 eV (775 nm) coupled to a Helios detection scheme from Ultrafast Systems. The fundamental (150 fs width, 1 kHz repetition rate) was split to provide both pump and probe pulses. Pump pulses were obtained by frequency doubling most of the fundamental to obtain 3.2 eV (387 nm) light. The remainder was passed through a sapphire plate to generate white-light probe pulses. Pump fluences varied between 2 to 100 $\mu\text{J}/\text{cm}^2$ with beam cross sections of $\sim 0.05 \text{ cm}^2$. TDA samples were prepared by mixing part of a NW stock with a solution of polystyrene in toluene (20% by weight). The sample was then dried overnight at the bottom of a quartz cuvette to obtain a smooth film.

Emission lifetime measurements

Excited state lifetimes were taken on the homebuilt microscope described above. All measurements were carried out on fused silica substrates in air. Excitation pulses had a duration of 70 ps at a repetition rate of 10 MHz (PicoQuant LDH-P-C 405). Crossed polarizers were used to attenuate their intensity. The resulting NW emission was passed through a barrier filter (Chroma, HQ 680LP) and was detected with a single photon counting APD (PicoQuant, PDM series). Its output was fed into a commercial time-correlated single photon counter (PicoQuant, PicoHarp 300). In this configuration, the largest contribution to the ~ 100 ps instrument response was the diode laser's pulsewidth (70 ps).

Conclusion

Through the concerted use of several ensemble and single NW experiments we have begun to develop a more comprehensive description about the nature of carriers and their recombination dynamics in CdSe nanowires. Among the conclusions found, we suggest that photogenerated carriers in larger diameter NWs predominantly consist of free electrons and holes. This accounts for the super linear growth of I_{emm} as a function of I_{exc} . At the same time, it also accounts for the excitation intensity dependence of the NW QY . Order of magnitude discrepancies between TCSPC and TDA kinetics are also rationalized through fast hole trapping and the existence of long lived electrons in the NW conduction band. These explanations are further supported by a kinetic model we have developed that reproduces our experimental observations. These insights add to our basic understanding about semiconductor nanowire photophysics and may ultimately aid their future use in NW-based applications.

Acknowledgements

We thank Jay Giblin for assisting us with the emission measurements as well as with subsequent absorption cross section calculations. B. J. and M. K. acknowledge financial support from the NSF NIRT program (ECS-0609249). M. K. also acknowledges support from the NSF CAREER program (CHE-0547784) and Research Corporation. Partial funding by the Notre Dame Radiation Laboratory, DOE Office of Basic Energy Sciences, is acknowledged.

References

-
- ¹ J. F. Wang, M. S. Gudiksen, X. F. Duan, Y. Cui, and C. M. Lieber, *Science* **293**, 1455 (2001).
 - ² Y. Yu, V. Protasenko, D. Jena, H. L. Xing, and M. Kuno, *Nano Lett.* **8**, 1352 (2008).
 - ³ X. F. Duan, Y. Huang, R. Agarwal, and C. M. Lieber, *Nature*, **421**, 241 (2003).
 - ⁴ R. Agarwal, C. J. Barrelet, and C. M. Lieber, *Nano Lett.* **5**, 917 (2005).
 - ⁵ J. C. Johnson, H. J. Choi, K. P. Knutsen, R. D. Schaller, P. D. Yang, and R. J. Saykally, *Nature Materials* **1**, 106 (2002).
 - ⁶ X. F. Duan, Y. Huang, Y. Cui, J. F. Wang, and C. M. Lieber, *Nature* **409**, 66 (2001).
 - ⁷ Y. Huang, X. F. Duan, Y. Cui, L. J. Lauhon, K. H. Kim, and C. M. Lieber, *Science* **294**, 1313 (2001).
 - ⁸ M. Law, L. E. Greene, J. C. Johnson, R. Saykally, and P. D. Yang, *Nature Materials* **4**, 455 (2005).
 - ⁹ Y. Yu, P. V. Kamat, and M. Kuno, *Adv. Funct. Mat.* **20**, 1464 (2010).
 - ¹⁰ Z. Zanolli, B. A. Wacaser, M. Pistol, K. Deppert, and L. Samuelson, *J. Phys. Cond. Mat.* **19**, 295218 (2007).
 - ¹¹ J. A. Goebel, R. W. Black, J. Puthussery, J. Giblin, T. H. Kosel, and M. Kuno, *J. Am. Chem. Soc.* **130**, 14822 (2008).
 - ¹² Z. Li, X. Ma, Q. Sun, Z. Wang, J. Liu, Z. Zhu, S. Z. Qiao, S. C. Smith, G. Lu, and Alf Mews, *Eur. J. Inorg. Chem.* **ASAP**, 4325 (2010).
 - ¹³ A. L. Efros, M. Rosen, M. Kuno, M. Nirmal, D. J. Norris, and M. G. Bawendi, *Phys. Rev. B* **54**, 4843 (1996).
 - ¹⁴ V. I. Klimov, *J. Phys. Chem. B* **104**, 6112 (2000).

-
- ¹⁵ J. J. Glennon, R. Tang, W. E. Buhro, R. A. Loomis, D. A. Bussian, H. Htoon, and V. I. Klimov, *Phys. Rev. B* **80**, 081303 (2009).
- ¹⁶ H. Yu, J. Li, R. A. Loomis, P. C. Gibbons, L. Wang, and W. E. Buhro, *J. Am. Chem. Soc.* **125**, 16168 (2003).
- ¹⁷ J. J. Glennon, R. Tang, W. E. Buhro, and R. A. Loomis, *Nano Lett.* **7**, 3290 (2007).
- ¹⁸ I. Robel, B. A. Bunker, P. V. Kamat, and M. Kuno, *Nano Lett.* **6**, 1344 (2006).
- ¹⁹ V. Protasenko, S. Gordeyev, and M. Kuno, *J. Am. Chem. Soc.* **129**, 13160 (2007).
- ²⁰ V. Protasenko, K. Hull, and M. Kuno, *Adv. Mat.* **17**, 2942 (2005).
- ²¹ V. Protasenko, D. Bacinello, and M. Kuno, *J. Phys. Chem. B* **110**, 25322 (2006).
- ²² J. Giblin, M. Syed, M. T. Banning, M. Kuno, and G. Hartland, *ACS Nano* **4**, 358 (2010).
- ²³ A. Lan, J. Giblin, V. Protasenko, and M. Kuno, *Appl. Phys. Lett.* **92**, 183110 (2008).
- ²⁴ J. Giblin, V. Protasenko, and M. Kuno, *ACS Nano* **3**, 1979 (2009).
- ²⁵ R. Zhou, H. Chang, V. Protasenko, M. Kuno, A. K. Singh, D. Jena, and H. L. Xing, *J. Appl. Phys.* **101**, 073704 (2007).
- ²⁶ J. W. Grebinski, K. L. Richter, J. Zhang, T. H. Kosel, and M. Kuno, *J. Phys. Chem. B* **108**, 9745 (2004).
- ²⁷ J. J. Glennon, W. E. Buhro, and R. A. Loomis, *J. Phys. Chem. C* **112**, 4813 (2008).
- ²⁸ M. C. Tamargo, "II-VI Semiconductor Materials and their Applications
Optoelectronic Properties of Semiconductors and Superlattices, Volume 12", Taylor and Francis, 2002.
- ²⁹ A. Shabaev, and A. L. Efros, *Nano Lett.* **4**, 1821 (2004).

-
- ³⁰ E. A. Muljarov, E. A. Zhukov, V. S. Dneprovskii, and Y. Masumoto, Phys. Rev. B **62**, 7420 (2000).
- ³¹ J. Puthussery, T. H. Kosel, and M. Kuno, Small **5**, 1112 (2009).
- ³² H. Htoon, J. A. Hollingsworth, R. Dickerson, and V. I. Klimov, Phys. Rev. Lett. **91**, 227401 (2003).
- ³³ J. W. Grebinski, K. L. Hull, J. Zhang, T. H. Kosel, and M. Kuno, Chem. Mat. **16**, 5260 (2004).
- ³⁴ M. Kuno, Phys. Chem. Chem. Phys. **10**, 620 (2008).
- ³⁵ A. Dong, R. Tang, and W. E. Buhro, J. Am. Chem. Soc. **129**, 12254 (2007).
- ³⁶ K. L. Hull, J. W. Grebinski, T. H. Kosel, and M. Kuno, Chem. Mat. **17**, 4416 (2005).
- ³⁷ M. Kuno, O. Ahmad, V. Protasenko, D. Bacinello, T. Kosel, Chem. Mat. **18**, 5722 (2006).
- ³⁸ J. Bellessa, V. Voliotis, T. Guillet, D. Roditchev, R. Grousseau, X. L. Wang, and M. Ogura, Eur. Phys. J. B **21**, 499 (2001).
- ³⁹ A. Saxena, S. Yang, U. Philipose, and H. E. Ruda, J. Appl. Phys. **103**, 053109 (2008).
- ⁴⁰ D. E. Cooper, J. Bajaj, and P. R. Newman, J. Cryst. Growth **86**, 544 (1988).
- ⁴¹ J. Lee, N. C. Giles, D. Rajavel, and C. J. Summers, Phys. Rev. B **49**, 1668 (1994).
- ⁴² J. Puthussery, A. Lan, T. H. Kosel, and M. Kuno, ACS Nano **2**, 357 (2008).
- ⁴³ M. Shim, S. V. Shilov, M. S. Braiman, and P. Guyot-Sionnest, J. Phys. Chem. B **104**, 1494 (2000).
- ⁴⁴ D. S. Ginger, A. S. Dhoot, C. E. Finlayson, and N. C. Greenham, Appl. Phys. Lett. **77**, 2816 (2000).

-
- ⁴⁵ D. Magde, J. H. Brannon, T. L. Creemers, and J. Olmsted, *J. Phys. Chem.* **83**, 696 (1979).